

Relativistic 3D jet simulations for the X-ray binary SS433

Remi Monceau-Baroux¹, Rony Keppens¹, Zakaria Meliani², and Oliver Porth^{1,3}

¹ Centre for mathematical Plasma Astrophysics, Department of Mathematics, KU Leuven, Celestijnenlaan 200B, 3001 Heverlee, Belgium

² LUTh, Observatoire de Paris, France

³ Department of Applied Mathematics, The University of Leeds, Leeds, LS2 9JT

Preprint online version: November 9, 2018

ABSTRACT

Context. Modern high resolution observations allow to view closer into the objects powering relativistic jets. This is especially the case for SS433, an X-ray binary from which a precessing jet is observed down to the sub-parsec scale.

Aims. We want to study full 3D dynamics of relativistic jets associated with Active Galactic Nuclei (AGN) or X-ray binaries (XRB). In particular, we study the precessing motion of a jet as a model for the jet associated with the XRB SS433. Our study of the jet dynamics in this system focuses on the sub-parsec scales. We investigate the impact of jet precession and the variation of the Lorentz factor of the injected matter on the general 3D jet dynamics and its energy transfer to the surrounding medium. Next to visualizing and quantifying jet dynamics, we aim to realize synthetic radio mapping of the data, to compare our results with observations.

Methods. For our study we use the code MPI-AMRVAC with relativistic hydrodynamic model of a baryonic jet. We use a block-tree adaptive mesh refinement scheme and an inner time-dependent boundary prescription to inject precessing bipolar super sonic jets. Parameters extracted from observations were used. 3D jet realizations that match the kinetic flux of the SS433 jet are intercompared, which vary in density contrast and jet beam velocity. We track the energy content, as deposited in different regions of the domain affected by the jet. Our code also follows the evolution of the energy distribution function for a population of particles injected with the jet. This evolving energy spectrum of accelerated electrons, using a pressure based proxy for the magnetic field, allows to obtain the radio emission from our simulation.

Results. we obtain meaningful observations of high resolution full 3D relativistic jet, both precessing and non-precessing. We find increased energy transfer for a precessing jet compared to a standing jets with otherwise identical parameters. We obtain synthetic radio maps for all jets.

Conclusions. The synthetic radio map matches best for a model using the canonical propagation speed of $0.26c$, and a 20° precessing jet. Overdense precessing jets experience significant deceleration in their propagation through the ISM, and while the overall jet is of helical shape. This argument shows that the kinematic model for SS433 assuming ballistic propagation has to be corrected for this deceleration.

Key words. Galaxies: jets, Hydrodynamics, Relativistic processes

1. Introduction

Non-relativistic up to highly relativistic jets are associated with a wide range of astrophysical objects. They can manifest themselves as a young stellar jet flow, or show up as (electromagnetically driven) jets or winds found in radio pulsars. High luminosity jets are detected through radio observations from active galactic nuclei (AGN) and from X-ray binaries (XRB), with the latter also denoted as microquasar systems. A review of those jets and their different origins and similarity can be found in Livio (2000). The study of AGN and XRB jets are related, and of utmost interest as their high kinetic influx in their surrounding is an efficient way to transfer energy from small structures to larger ones. Both AGN (see Silk & Rees (1998)) and XRB (see Fragos et al. (2013)) jets play a role for cosmological evolutions, by feeding back part of the accreted energy to the galaxy clusters. We aim to quantify, using numerical simulations, precisely this energy transfer from the jet to its surroundings. In previous work Monceau-Baroux et al. (2012), we studied the impact of varying the jet opening angle on the resulting jet dynamics. We here study a finite

opening angle jet, with a more dramatic temporal change: a precessional motion of the jet. This implies to drop the axisymmetry, commonly used in various studies on relativistic jet propagation and requires full 3D simulations. Such a precessing motion can be found in the SS433 XRB system.

SS433 was discovered in star surveys exhibiting $H\alpha$ emission in 1977 (see Stephenson & Sanduleak (1977)). It was observed that the emission in this system was Doppler shifted from the position $H\alpha$ emission is emitted in static material at this astrophysical distance. The emission line for SS433 is triple: one is shifted to the red, one to the blue and the third one is not shifted. This is the mark of a static object with two outflows: one oriented toward the observer, and one away. This feature appears in almost all objects associated with jets. But what is making SS433 unique is that the shift is evolving with time. Two years after it was discovered, many publications (see Fabian & Rees (1979), Milgrom (1979b), Milgrom (1979a) and Margon et al. (1979)) started investigating the periodic variation of its intensity. The first evidence of periodicity

was the 164 days variability. This was explained by the fact that the outflow was changing its position in time, and established the fact that SS433 had precessing bipolar jets. A first estimation of the jet lower velocity was calculated (see Fabian & Rees (1979)) and found to be relativistic and above $0.2c$. From emission line observations of SS433, observers refined the velocity for the material of the beam of $0.26c$ and its period to 162 days (see Milgrom et al. (1982)). These observational evidences lead to the kinematic canonical model for SS433: the jet precesses with a period of 162 days with a 20° precession axis, itself inclined by 78° from the line of sight (see fig. 1). Note that if the kinematic model adopts a constant relativistic speed, AGN jet simulations often compare propagation speeds with the 1D approximation of Marti from 1997 (see Marti et al. (1997)) based on ram pressure arguments, which distinguishes jet beam from jet head advance properties. Furthermore it is interesting that from this equation we can see how for a given kinetic energy flux of a jet, it is possible to obtain different combinations of density contrast and velocity of the jet matter, which still give the same speed of propagation for the jet head, due to interaction with the surroundings. We will revisit these findings for mildly relativistic jet models appropriate for SS433 and similar systems, to discuss how their jet deceleration varies with these parameters.

SS433 was quickly described as a binary system (see Margon (1984)) made of a giant star losing its material to its compact companion. The flowing material forms an accretion disk around the smaller partner. This disk give rise to a collimated jet. The mechanisms by which such jet arise are subject of many studies (see the review by Livio (2000) and Markoff (2006)) and will not be studied here. If this picture is widely accepted, the exact nature of the system is still discussed: evidence would suggest the compact object to be either a neutron star with a low mass or a black hole of mass superior to $4.3M_\odot$ (see Margon (1984)). More recent study suggests mass up to $16M_\odot$ (for a total mass of the system of about $40M_\odot$) (see Blundell et al. (2008)) and favor a black hole. The accretion disk is also expected to be of the same order of expansion as the size of the orbiting system: $10^{12}cm$ (see Krivosheyev et al. (2009)). It is thought that this accretion disk in SS433 is precessing around its compact central object. This disk is thought to be unaligned with the orbital plane of the binary. This is discussed in detail in Katz et al. (1982): they matched the shift of the emission lines of the source with the prediction from their models. This after removing the emission supposed to be coming from the jets. This in turn is thought to create the precessing motion of the jet. An additional nutation of the jet, with a period of 6.5 days can be linked to the orbital period of the binary, which is known to be 13 days. This figures and model are obtained from observations of the sources through the analysis of the occultation profile (see Margon et al. (1979), Crampton & Hutchings (1981)). When we adopt specific 3D jet morphologies inspired by these SS433 considerations, we wish to understand how the precession affect the energy transfer from the jet to its surroundings, as opposed to a static jet configuration.

Nowadays there exist abundant observations of all scales of SS433. From the large scales (20 pc) interaction of SS433 with the supernova remnant W50 (see Dubner et al. (1998)). Relativistic hydrodynamics simulation (see Zavala et al. (2008)) were aim to reproduce those observations and find a possible time dependant evolution

of the precessing angle for SS433 from 10 to 20° . For the smaller scales of SS433 observations (about 1 AU of the source of the jet), VLBA and VLBI give more insight on the close region of the binaries. This show a less continuous pattern with a high variability and X-ray and radio components being ejected from the central region (see Paragi et al. (1999)). A movie was release in 2004 showing the time dependent evolution of its emissions for 40 years (about $1/4$ of its period of precession). For the scales of our study of the order of $0.1pc$, we have radio observations. In particular the observations from the VLA observatory on which we can clearly see the helix pattern due to the precession (see Spencer (1979), Hjellming & Johnston (1981), Roberts et al. (2008)). Often such observation are over-plotted with the kinematic model widely adopted for SS433. This model assume a distance to SS433 of $5.5kpc$ (see Roberts et al. (2008)). While this agrees to a large extent, often small discrepancies arise between that model and observational details. We therefore also target to produce radio maps of our simulations in order to compare them to both observations and the standard kinematic model.

As for more recent studies on SS433, we founded many observational studies on the inner region of the object and circumstellar disk, mainly with the VLBA instrument, (see Marshall et al. (2013), Bowler (2013)). But little simulations works exist taking advantage of the increasing capabilities of modern simulation codes and clusters. In 2010 Muller & Brinkmann (2000) did a moderate resolution ($500 \times 120 \times 120$) non relativistic hydro 3D simulation with a one side jet. In 2008 Zavala et al. (2008) did a 3D simulation as seen above, on the interaction on large scales with the SNR W50. A few more 2D and 3D simulation exist on the flow of material from the massive star to the compact companion in the binary. Our work aims therefor to take advantage of the simulation tool to back up VLA observations of the intermediate scales of SS433 (about 0.1 parsec) and in future work of more time variable smaller scales VLBA observations.

In the following, we will first introduce our method: the models and simulations we used for both hydrodynamics simulation and radio mapping. This section will also present the tools and diagnostics used for the study of the simulations. The presentation of our result will then be divided in three sections: first a visual description of the different cases and make some first remarks and observations. We will continue with the results of a series of diagnostic run on our simulations which will give us insight into the energy transfer between the jet and its surroundings and on the role of the precession versus the variation of the free parameters in our model. The third part of our result will present the radio maps we produced and compare them to similar radio observations of SS433. We will finally give some general conclusions of this work.

2. Simulation aspects

Like in our previous works (Monceau-Baroux et al. 2012; Meliani et al. 2008), we use a relativistic hydrodynamic model with the relativistic variant of the Euler equations, with the Mathews approximation (see Blumenthal & Mathews (1976)) to the Synge gas relation as a closure. The calculations are performed in a 3D cartesian grid with a domain spanning $0.2 \times 0.1 \times 0.1 pc^3$ using

open boundary conditions on all sides. The bipolar jet is injected time-variable from the center of this domain, using an inner spherical region as a boundary zone, where we at each time fully prescribe all variables within a sphere of radius 0.008 pc. As a result, the source itself is left out of the simulation. This is important for the radio mapping of the simulation, as we will see later. We first briefly discuss the numerical approach, for both the gas dynamical and the radio mapping part, and then explain how we initialize and further analyze the data.

2.1. Code and implementation

We use MPI-AMRVAC¹ (Keppens et al. 2012), to numerically integrate the relativistic HD equations. As explained further on, additional equations are solved concurrently, for evolving the electron distribution and for passive tracers, which are all easily incorporated in the open source software².

Our simulations use a TVDLF solver with a threestep time discretisation (see Tóth & Odstrčil (1996)), where a up to third order spatial reconstruction is done with a Koren limiter (see Koren (1993)). We are using a block-based adaptive mesh refinement (AMR) scheme to have full resolution only where needed. We start with a base resolution of $144 \times 72 \times 72$ and allow for 4 levels of refinement, which gives us an effective resolution of $1152 \times 576 \times 576$ (corresponding in our case to cells of $(1.736110^{-4})^3 pc^3$). The AMR is triggered automatically by following the evolution of density, pressure and Lorentz factor. Additionally we always enforce maximal refinement around the central source region of our jet. Simulation cases A, B and C (see later on) exploit typically 512 CPUs for 40 hours, case D completed in 20 hours.

2.2. Model for radio mapping

Our method for radio mapping is based on the work of Camus et al. (2009) and was implemented to MPI-AMRVAC in Porth et al. (2013), submitted to MNRAS. During the simulation we follow the evolution of a passive electron distribution which has an energy power law $\epsilon^{-\Gamma_e}$ dependence for energies $\epsilon \leq \epsilon_\infty$, with fixed $\Gamma_e = 0.6$. The initial cutoff energy injected with the jet is $\epsilon_{\infty,0} = 1\text{TeV}$. Three dynamically evolved quantities are added to the simulation, namely $\rho_e(\mathbf{x}, t)$, the electron density at time t ; $\rho_{e0}(\mathbf{x}, t)$, the advected initial electron density for the evolved population; and $\epsilon_\infty(\mathbf{x}, t)$ the cutoff energy. ρ_{e0} simply follows a pure advection equation, and is set to initial density values $\rho_{e0} = 1cm^{-3}$ in the jet and $10^{-5}cm^{-3}$ everywhere else. ρ_e follows a conservation law and ϵ_∞ is evolved to account for adiabatic losses. Since we do not evolve the magnetic field, the synchrotron losses of ϵ_∞ are neglected in this work.

In post-processing we start by reconstructing a new 3D box oriented with respect to the line of sight from the observer. The angle $\theta = 78^\circ$ between the axis of precession and the line of sight is obtain from radio observation (see Margon (1984)). This box has a resolution of $64 \times 128 \times 64$ and is filled by interpolation of the data from the simulation onto the new box. We calculate the synchrotron emissivity

in the observer's frame in this new box using equation (7) from Camus et al. (2009)

$$E_{\text{miss}} = \rho_{e0} D^2 B_\perp \left(\frac{\rho_{e0}}{\rho_e} \right)^{-\frac{\Gamma_e+2}{3}} \epsilon^{1-\Gamma_e} \left(1 - \frac{\epsilon}{\epsilon_\infty} \right)^{\Gamma_e-2}, \quad (1)$$

where B_\perp is the component of the magnetic field normal to the line of sight in the fluid frame and

$$D = \frac{\nu_{\text{obs}}}{\nu} = \frac{1}{\gamma - \mathbf{k} \cdot \frac{\mathbf{v}}{c}}, \quad (2)$$

is the Doppler factor with \mathbf{k} the vector of the line of sight, γ the local lorentz factor, ν_{obs} the observed frequency and ν the emitted frequency. The latter is expressed as $\nu = (3e/4\pi m^3 c^5) B_\perp \epsilon^2$, where e and m are the electron charge and mass. Our simulation does not include the magnetic field, and the 3D geometry of the problem does not suggest a simple magnetic field topology. Still, we make the approximation to consider weak frozen in magnetic field, meaning that in the previous equation B_\perp is taken equal in intensity to the square root of the local thermic pressure value \sqrt{P} (matching magnetic and thermic pressure) time a scaling constant. After making the assumption that we have an optically thin medium, we can sum the emissivity along the direction of the line of sight. We then obtain a 2D intensity radio map for the object with

$$I(x, y) = \int_{\text{LOS}} E_{\text{miss}}(x, y, z) dl. \quad (3)$$

To be able to compare our map with observations from a specific telescope, we finally apply a beaming effect with respect to the characteristics of the instrument. This is done by convoluting the emission map with a gaussian of 0.01pc full width at half maximum (FWHM instrumental convention). This corresponds to the VLA observation restoring beam as used in the observations used in Roberts et al. (2008).

One important note is that we only simulate the propagation of the jet and not the central object. As a direct result, the bright central object does not appear on our radio maps. To correct for this, we add a bright pixel at the center of our radio map before applying the beaming. We take the un-resolved flux of that central source to be equal to a fraction of the flux of the obtained map. To empirically matched the apparent ratio between the source and the jet from VLA observation, this fraction is taken to be one fourth.

2.3. Initial conditions

We extract as many parameters from observation as possible, and collect them in Table 1. These are identical for all runs, and set (1) the thermodynamic conditions of the ISM in terms of pressure and density $P_{\text{ISM}}, \rho_{\text{ISM}}$ (Safi-Harb & Ogelman (1997)); (2) the energy flux of the jet L_{kin} (Brinkmann et al. (2005)), which appears to be average for an XRB jet; and (3) the jet half opening angle α_j which we set to 5° . Note that observations give a half opening angle for the jet of 1.2° , we use here a value of 5° as an average for incorporating the fast nutation of the jet with period $T_{\text{nut}} = 6\text{days} \ll T_{\text{prec}} = 162\text{days}$ adding an extra 3.5° . For both jet opening angle and nutation angle see Collins & Newsom (1979), Margon (1984) and Borisov & Fabrika (1987).

¹ Code homepage at homes.esat.kuleuven.be/~keppens/

² GIT repository at [gitorious.org/amrvac/amrvac](https://github.com/gitorious.org/amrvac/amrvac)

L_{kin}	r_b	ρ_{ISM}
$10^{39} \text{ erg.s}^{-1}$	0.0007 pc	$8.3 \times 10^{-24} \text{ g.cm}^{-3}$
P_{ISM}	T_{prec}	Base resolution
$7.5 \times 10^{-6} \text{ g.cm}^{-1} \cdot \text{s}^{-2}$	162 days	$144 \times 72 \times 72$
Domain size (pc)	α_j	Effective resolution
$[-0.1, 0.1]$	\times	5°
$[-0.05, 0.05]$	\times	$1152 \times 576 \times 576$
$[-0.05, 0.05]$		

Table 1. General parameters for all simulations. See section 2.3 for references and a more detailed description.

Case	$\gamma_b (v_b)$	Inertia ratio	θ_{prec}
A	1.036 (0.26c)	28.6	20°
B	1.87 (0.845c)	0.8	20°
C	1.036 (0.26c)	28.6	10°
D	1.87 (0.845c)	0.8	0°

Table 2. Parameters for the simulations which vary from case to case.

In Monceau-Baroux et al. (2012) we were fixing the density ratio between an injected jet beam and its ISM and derived all other quantities from the given kinetic energy content. Here, we rather fix the value of the jet Lorentz factor γ_b . Knowing the integrated energy flux over the beam cross section relates to dynamic parameters as

$$L_{kin} = (\gamma_b h_b - 1) \rho_b \gamma_b \pi r_b^2 v_b, \quad (4)$$

where ρ_b, r_b, v_b are the jet beam density, radius and velocity, while $\rho_b h_b = \rho_b + \frac{\Gamma}{\Gamma-1} P_b$ is the enthalpy for a given polytropic index Γ . P_b is chosen at the injection surface to be equal to the ISM pressure P_{ISM} . Knowing Γ the relativistic hydrodynamic equation, we can obtain ρ_b . Table 2 gathers the imposed and derived parameters which differ from case to case. Here the inertia ratio, defined as $\eta = \gamma^2 \frac{\rho_b h_b}{\rho_{ISM} h_{ISM}}$ gives an indication of the difference of conditions between the jet and its surroundings.

The injection of the bipolar jet is realized by overwriting at each time step the values within a sphere of radius $r_0 = 0.008 \text{ pc}$ at the center of our domain as seen on Figure 1. We identify the cone of the jet at each time by finding its axis position,

$$\mathbf{OJ} = \mathbf{OP} + \mathbf{PJ}, \quad (5)$$

with O the central source of the jet, P a fixed point on the precession axis and J a point on the axis of the jet. \mathbf{OP} is static in time and J has a circular motion around P with period 162 days and radius $r_{prec} = \|\mathbf{OP}\| \tan \theta_{prec}$. Having obtained the instantaneous orientation axis of the jet \mathbf{OJ} we define the cone using cylindrical coordinates (r, θ, z) , oriented with the z -axis defined by this jet axis. The jet interior obeys $r \leq |z| \tan \alpha_j$. In Figure 1, the (half) jet cone is drawn where this cone intersects the sphere of radius r_0 , and together with the jet opening angle, this determines the jet radius on entry r_b . We obtain the bipolar jet by simply applying this to negative z . Velocity vectors within the precessing cone are purely radial and the density ρ is defined

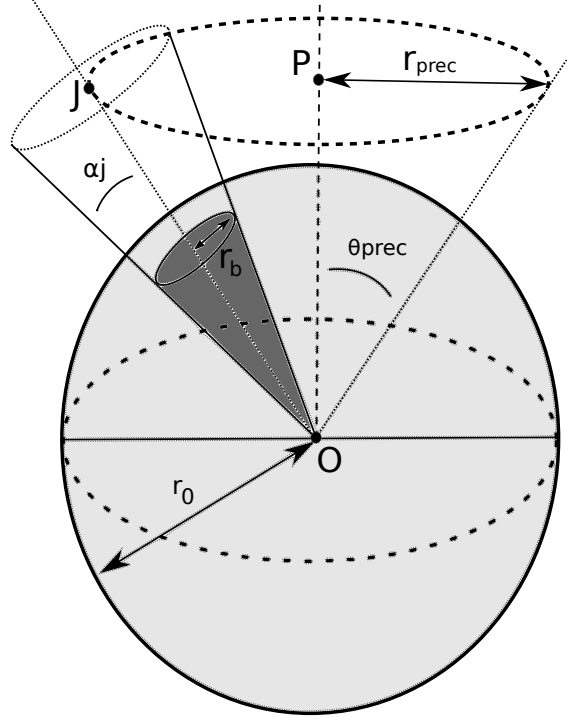


Fig. 1. Geometry used for the inner boundary jet injection prescription.

in the cone of the jet as $\rho(r) = r_0^2 \rho_b / r^2$, with ρ_b the density as calculated from equation 4. The pressure P is defined in the cone as $P(r) = r_0^2 P_b / r^2$ with $P_b = P_{ISM}$. The later use the assumption that only pressure matched jet can propagate into the ISM dominated by kinetic processes. The rest of the domain is set to a uniform ISM, as is the part of the central overwritten sphere outside the bipolar jet cone. All parameters for the initial condition and the geometry for all cases can be found in table 1 and table 2.

2.4. Data analysis

To identify at all times the different regions of the domain as affected by jet propagation, we use two complementary methods. A passive tracer follows the evolution of the jet and allows us to locate purely jet beam material. The second method, as earlier introduced for our axisymmetric jet simulations in Monceau-Baroux et al. (2012), uses instantaneous versus initial conditions of the data to locate the entire region altered by jet passage. The tracer is passively evolved with respect to the flux of density, hence

$$\nabla_\mu (\rho \rho_{tr} u^\mu) = 0. \quad (6)$$

It is set to the density value in the injection region of the jet and 0 elsewhere. We can then identify the beam of the jet where matter from the jet is $\rho_{tr} \geq 0.1 * \rho_{tr0}$. This is the filter used to find the instantaneous most remote position of the head of the jet: $r_{head}(t)$ indicates the furthest radial distance from the central source where jet beam matter exists. Note that for the precessing case, we do not clearly observe the formation of a Mach disk as found in the study of non-precessing AGN jets or in our case D. Where the value of the tracer is non zero and $\rho_{tr} 0.1 * \rho_{tr0}$, we find the entire jet cocoon, which gives us also the position

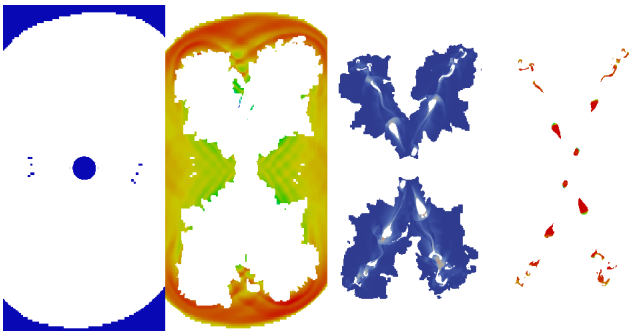


Fig. 2. Filter for the decomposition of the regions of the domain. Case A, time $t = 1$. From left to right we identify in a cross-sectional plane the unaffected ISM, the shocked ISM, the jet cocoon, and the jet beam.

of the discontinuity between mixed matter from jet and ISM and the shocked interstellar medium (SISM): hence $r_{\text{disc}}(t)$ is the maximal radial distance where the jet cocoon extends to at a certain time t . The shocked ISM is then found from all regions where the energy excess is not zero. This energy excess is defined as the difference between the local energy (thermal and kinetic) at the observed time, and the energy at the same location in the initial condition $E_{\text{excess}}(\mathbf{x}, t) = E_{\text{tot}}(\mathbf{x}, t) - E_{\text{ini}}(\mathbf{x}, t = 0)$, with $E_{\text{tot}} = E_{\text{therm}} + E_{\text{kin}}$ the total instantaneous energy summing up kinetic and thermal energy. Note that this excess energy is the energy measure used later on in section 3.2, for energy transfer quantifications. $E_{\text{ini}} = E_{\text{therm,ini}} + E_{\text{kin,ini}}$ is the total energy at time $t = 0$ (note that at time $t = 0$ the kinetic term is non-zero only in the jet region as the overwritten sphere at the center of the domain is included in the calculation). This region gives us the position of the front shock, where $r_{\text{SISM}}(t)$ is once more the furthest radial distance found from this energy excess locator. In locating only shocked ISM regions, or only jet cocoon regions, we also make sure that the different regions do not overlap. This implies that we exclude the jet region from all other regions, and similarly exclude the cocoon from the shocked ISM and the shocked ISM from the unaffected ISM region. An example of a 2D cross section of such filtering for case A at time $t = 1$ can be seen on figure 2.

3. Results

3.1. General dynamics

The main feature of the jet associated with SS433 is its precessing motion. This raises the question whether there can be significant differences in dynamics between a static and a precessing jet. As we always consider finite opening angle, conical jet injections, our earlier work in Monceau-Baroux et al. (2012) provides a description of the expected hydrodynamics of a non precessing jet, although that work was focused on axisymmetric 2D jets associated with AGN. In the present case, we are working with a jet associated with an X-ray binary. However, it is generally accepted that even if those two cases have completely different scales and overall energetics, their dynamics are similar and the jets are in each case launched from (the central regions of) an accretion disk around a compact object like a black hole, fed by its surroundings (a galaxy for AGN or a mas-

sive companion for XRB). We recall that for non-precessing, steadily injected relativistic hydro jets, the interaction of the jet with its surroundings includes four important aspects: kinetic energy is transformed into thermal energy through internal shocks in the jet beam (also due to recollimation when injected at finite opening angle) and ahead of the jet at the overarching bow shock. The latter realizes a much more important fraction of the energy conversion. Within the shocked ISM medium, we find many traversing shocks, created at the dynamically evolving contact surface of interaction between the jet and its shocked surroundings, thereby heating the shocked ISM medium. Finally, many fluid instabilities (Kelvin-Helmholtz, Rayleigh-Taylor) develop around the jet, mixing together jet and ISM material. Our first approach to the case of the precessing XRB jet, is thus to directly compare it with a similar, but 3D static one, so that we can see which of those mechanisms are still present, and determine their relative importance.

For the rest of this general discussion, we focus on three of our cases: a precessing jet at the typically quoted SS433 jet speed, Case A ($\gamma = 1.036$), a precessing Case B at higher propagation speed, making the jet underdense ($\gamma = 1.87$) and its non-precessing analogue Case D ($\gamma = 1.86$). The comparison between the first two allows to obtain some insight on the effect of the Lorentz factor on the dynamics of a precessing jet, whereas comparing the last two cases allows for the study of precession itself on the dynamics of mildly relativistic jets. A global representative view on those three cases can be found in figure 3. The three cases are visualized at dimensionless time $t = 2$ of the simulation, which is 6.5 years in the full evolution. With the period of 162 days for the precession, this corresponds to 14.7 precession of the source. On a 2D plane cut we plotted density, while a volume rendering is realized by using the advected tracer described in section 2.4. On this volume we quantified pressure.

A first look at the three cases allows to draw a first set of observations: while the non precessing case D easily has propagated out of the limits of the simulation box after 7 years ($t = 2$), both cases A and B are still fully contained within the domain, with A having reached further than B. The general shape of the jet is fundamentally different between the precessing and non precessing jets: case D has an overall circular cross-section of its beam, well known from extensive studies of relativistic jets of AGN or XRB. The precessing cases on the other hand have a helical beam which has a ribbon-like appearance with a low pressure extended part at the back of each annulus. The front side of the annuli display a high pressure zone. We argue that this pressure pattern is comparable with that associated to a propagating piston: high pressure builds in front of the piston while the pressure drops behind it due to adiabatic expansion. Since the size of the simulation box is set to be $0.2 \times 0.1 \times 0.1 \text{ pc}^3$, with a ballistic propagation where we simply adopt the beam velocity v_b , case A and B would cover the 0.1 pc of its maximal expansion in respectively 1.25 and 0.39 year, with 2.8 and 0.9 precessions completed along the way. Both simulations display more than that number of windings through the box, and experienced more precession on both side of their propagation. For case A, we can clearly see 4 complete windings of precession (648 days) so that the same distance of 0.1 parsec suggests an overall jet speed of propagation of $v_{\text{head}} = 0.185c$ (with c

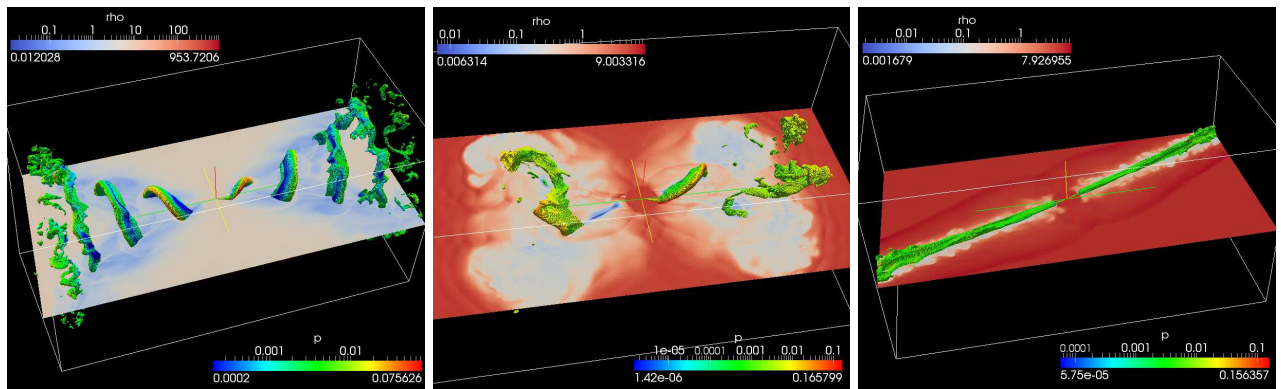


Fig. 3. Global view of three cases at times $t = 2$ (6.53 years) for case A and B and time $t = 0.25$ (0.82 year) for case D. Density is shown on a 2D cut. The jet beam is drawn where $\rho_{\text{frac}} > 0.8$. The pressure is quantified on the jet beam surface. Left: Case A $\gamma = 1.036$; Middle: Case B $\gamma = 1.87$; Right: Case D $\gamma = 1.87$, no precession.

the speed of light). This is a clear first hint for deceleration experienced by the precessing jet.

As in the case of AGN jets, one of the main parameters for determining the propagation speed of the jet through the medium, is the inertia ratio between the jet and the medium $\eta = \gamma_b^2 \frac{\rho_b h_b}{\rho_{ISM} h_{ISM}}$. The ram pressure, which is the force felt by the jet and opposing its propagation, is exerted along the axis of propagation and is as $F_{\text{ram}} \propto -\rho_{ISM} \gamma^2 v_b^2$. To find an approximation to the resulting deceleration, we take the relativistic correction to the second law of Newton (in the parallel direction) valid for low γ : $F_{\text{ram}} = \gamma^3 \rho_b a$. We then find for the deceleration $a = -\rho_{ISM} v_b^2 / \rho_b \gamma$ where v_b , ρ_b and γ are linked through equation 4. This shows that the response of the deceleration to the variation of γ is not a simple linear relation.

For a non precessing jet, it is expected that a higher density ratio results in a more effective deceleration (see Marti et al. (1997)). For a 1D jet, ram pressure balance allows to obtain the equation $v_{\text{head}} = \frac{\sqrt{\eta}}{\sqrt{\eta+1}} v_b$ where v_{head} is the speed of propagation of the head of the jet, v_b the velocity of the material in the beam of the jet and η is the inertia ratio between the beam with density ρ_b and enthalpy h_b , and the ISM with density ρ_{ISM} and enthalpy h_{ISM} . Following that equation, a theoretical expected velocity for the jet head is $v_{\text{head}}^{\text{marti}} = 0.22c$, which is higher than the $v_{\text{head}} = 0.185c$ we previously deduced.

Case D displays a narrow cocoon around its beam with mixing of material between shocked ISM and jet matter. That mixing is also present for the two precessing cases. However, case A shows a somehow similarly narrow cocoon, while case B inflates a wide bubble of low density material. Only within that cocoon does the jet for case B assume the typical helix shape. The difference between cases B and D, which have the same density ratio, can be explained by their difference in interaction with the ISM. Due to its precession, case B has a much larger interaction surface than case D. More energy is then transferred to the cocoon for case B, inflating it more than for cases D or A.

The continuous injection regime inside the static jet case D allows for the formation of standing shocks along the path of the jet. Those shocks are the result of recollimation of the jet by the interaction with the surroundings through ram pressure, as already found in axisymmetric studies. These recollimation shocks are virtually absent in the precessing

jets. As a result, if we still expect ram pressure to play a role for collimation of precessing jets, the inertia contrast will to be the main way to keep a jet collimated. The inertia of the jet at the injection surface is linked to its density ρ_b , itself linked to the Lorentz factor, as seen before. We mentioned that for the same kinetic flux of the jet, we can adopt different inertia and Lorentz factor combinations, which is why we included the study of the effect of the variation of γ_b on the collimation of the jet.

3.2. Quantification of dynamics

We now obtain quantified information on the different cases. Figure 4 gathers such results: on the top row we show the maximal velocity profile at different times for cases A, B and D. This velocity depends on the radial distance to the source of the jet and quantifies at each radius $v_b(r) = \max(v(r))$. We note that this $v_b(r)$ is giving the highest velocity value found on a sphere of radius r to the central source point, and not the always maps on the value of the velocity of the jet at distance r . One of the consequences of its definition is that the two oppositely directed jets both contribute to this measure. By using the method described in section 2.4, we also show the spatial reach of the jet head, the contact discontinuity and the front shock as a function of time, in the bottom row panels.

The first information given by both velocity profile evolutions and radial reaches is on the propagation of the head of the jet. The width measurements give us insight on the temporal evolution of the actual head velocity v_{head} , the speed of the discontinuity v_{disc} and front shock v_{SISM} , as derivatives of the $r_{\text{head}}(t)$, $r_{\text{disc}}(t)$ and $r_{\text{SISM}}(t)$ profiles. The radial velocity profiles give us information on the internal spatial distribution of the beam velocity v_b . Note that due to their differences in dynamics, the figures are shown up to time $t = 0.25$ (0.82 year) for case D, and up to time $t = 2$ (6.53 years) for both case A and B.

Case D (no precession, $\gamma = 1.87$) shows always a very sharp velocity profile: its maximal velocity remains nearly constant all along its beam and drops abruptly at the position of its head. Its head propagates in accord with the Marti 1D model (see Marti et al. (1997)) prediction with no Ω correction (see section 3.1). Its beam has a velocity of $v_b = 0.845c$ and its head propagates with $v_{\text{head}} =$

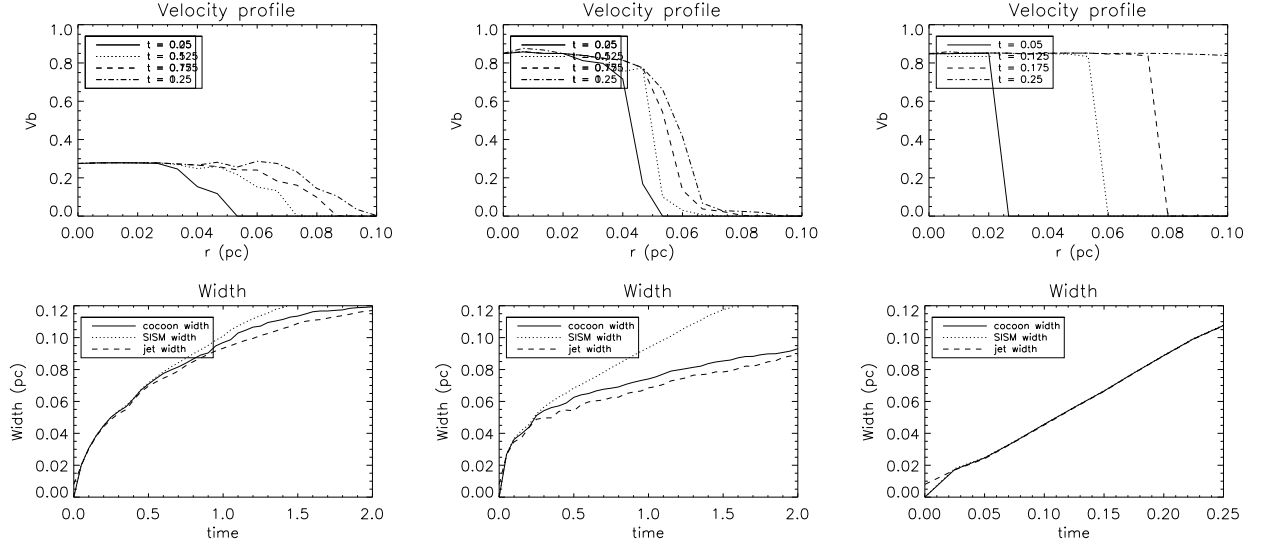


Fig. 4. Top: Radial speed profiles for various times. Bottom: furthest radial reach of SISM, cocoon and jet regions. Left: Case A $\gamma = 1.036$; Middle: Case B $\gamma = 1.87$; Right: Case D $\gamma = 1.87$, no precession.

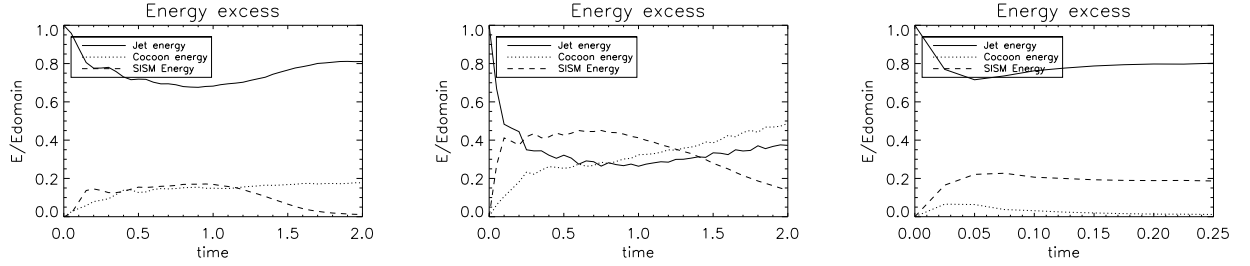


Fig. 5. Energy transfer evolution as functions of time. Left: Case A $\gamma = 1.036$; Middle: Case B $\gamma = 1.87$; Right: Case D $\gamma = 1.87$, no precession.

$v_{SISM} = v_{marti} = 0.39c$. This case is a canonical underdense relativistic jet, really similar to a scaled down AGN jet. A closer look to this flat velocity profile (fig. 6) reveal the internal structure of the jet. We can see the formation of the first three standing recollimation shocks at distance 0.02 pc, 0.047 and 0.07 pc. As shown before, case A (precession, $\gamma = 1.036$) does not follow the same model and is further decelerated. Its radial velocity profile also shows that its deceleration does not only take place at its head, but all along its beam: closer to the center, its $v_b(r)$ remains unchanged before smoothly decreasing over a large distance. The width of this transition region increases with time: for case A, $0.03pc$ at time $t = 0.25$ and $0.045pc$ at time $t = 1$ (3.26 years). We later on associated that transition region with the SISM region. Where case D follows v_{marti} , this is not the case for case B ($v_{marti} = 0.39c$) and case A ($v_{marti} = 0.22c$).

For all cases, at early times, the jet induces the front shock to form and push it. This result the front shock to propagated at the same speed as the jet head own supersonic speed (mach number relatively to the ISM sound speed: $M = 6$ for case A and $M = 22$ for cases B and D). Then the position of the front shock and the jet head become disconnected as the jet head gets decelerated to subsonic velocity (the jet beam matter staying supersonic).

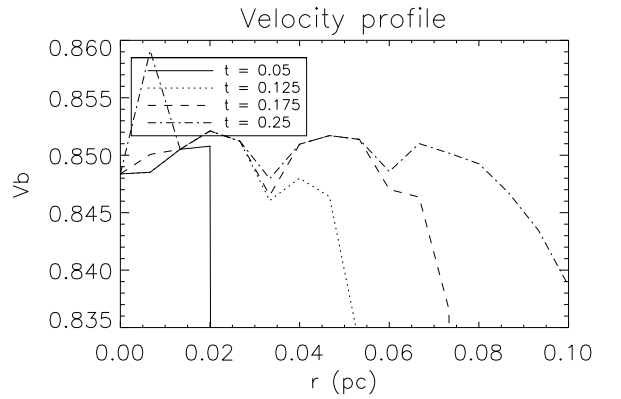


Fig. 6. Internal structure of the non precessing case D. Internal structure appear with standing recollimation shock at 0.02 pc, 0.047 and 0.07 pc

Case D, as seen before, follows a bullet-like propagation, and we do not observe a clear disconnection between the three regions by our method during the simulation time. Case A disconnects at time $t = 0.5$ and case B at time $t = 0.25$. The velocity of the front shock of the two last

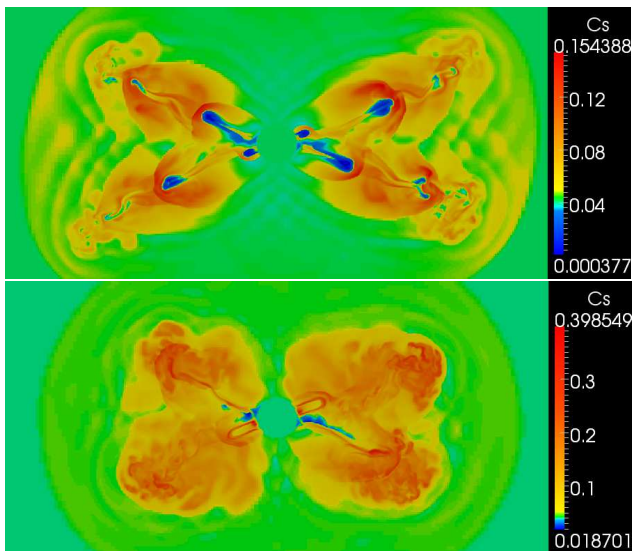


Fig. 7. 2D cut of the domain, mapping of c_s at time $t = 1$. Top: case A; Bottom: case C

cases were fitted with the same $v_{head} = 0.05c$ which is higher than the ISM sound speed $c_{s,ISM} = 0.04c$. By plotting the sound speed over a 2D cut of the domain (figure 7), we see in both cases A and B that the sound speed inside the cocoon is higher than the ISM sound speed ($c_{s,cocoon} > c_{s,ISM} = 0.04c$). The sound speed in the jet region can go above $0.1c$ where in the SISM region it is on average around the measured velocity for the front shock. The discontinuity between the cocoon and the ISM, simply propagated a short distance in front of the transfer surface after it disconnected from the front shock. We recall that this transfer surface between the jet matter and the cocoon is the location of the conversion from kinetic to thermal energy. Both discontinuity and transfer surface have comparable velocity. This is expected from simple 1D model of relativistic jets. A similar behavior is also present in 2D relativistic jets (see Monceau-Baroux et al. (2012)). In the axis of propagation direction, the discontinuity is propagating at constant distance from the transfer surface, of Mach disk in the case of static jets.

By looking at the velocity profile (top row of fig. 4), we can see that it has a third regime after the flat undecelerated profile near the origin, and the constant deceleration part: after a rapidly growing deceleration, the profile displays a knee where the deceleration softens. This is especially evident for case B: by taking the curve for time $t = 1$ one finds the knee to be at a distance of 0.065 pc and the end of the deceleration sits at 0.09 pc where the velocity profile reaches zero. By looking now at the graph of the radial reaches for the same case, we see that at time $t = 1$ the end of the jet beam and front shock position are found at respectively 0.065 pc and 0.09 pc. Therefore this region lies outside of the cocoon, in the SISM region. As the velocity is not null this is direct evidence that the SISM is accelerated to mildly relativistic speed ($0.03c$ for case B). Only shocks can bring energy to the SISM region and we know from previous studies (see Monceau-Baroux et al. (2012)) that this energy is mainly thermal. But we see here that they have to be the source of the acceleration and bring kinetic energy to the SISM. The same can be observed for case A.

For case D, as already mentioned, the Mach disk and the front shock are not clearly disconnected, thus this feature is absent.

In Figure 5, we used the method explained earlier to quantify energy deposition aspects. Two problems arise when considering the energy contents of the different region for our simulations. Firstly, we use a sharp initial profile in our initial condition from which both SISM and cocoon are ignored, with the jet being directly in contact with the unperturbed ISM at $t = 0$. As a result, the simulation needs some time to reach a more physical regime (estimated here for cases A, B and D to be respectively at times $t = 0.15$, 0.15 and 0.025). Secondly, to keep the simulation cost manageable, we used a rather small box with open boundaries allowing for dynamics to go through the continuous boundaries. This allows energy to leave the box at later times of the simulation (estimated here for cases A, B and D to be respectively at times $t = 1$, 1.2 and 0.23). This fact clearly appears in the energy graphs for cases A and B, where the fraction of excess energy present in the SISM part of the domain decreases rapidly when the SISM starts going through the boundaries when both jet and cocoon are still completely inside the domain. These two observations impair our energy measurements at later times. However, we can still make conclusions from the general trend of the energy graphs. The first evident conclusion is made by comparing case A and B. In case A most of the injected energy is remaining in the jet itself, far above both cocoon and SISM regions. In case B, the highest energy fraction is present in the SISM and then in the cocoon, with only one third of it remaining in the jet region. This is a direct consequence of the interaction between the jet and the ISM, as affected by jet precession and its inertia contrast. A much higher fraction of energy is transferred from the jet to the ISM as the Lorentz factor (case A: $\gamma = 1.036$; case B: $\gamma = 1.87$) increases. This is another means of verifying that case A propagated almost freely in the ISM whereas case B starts by inflating a hot cocoon in which it can then propagate. Both case A and D (with no precession for case D) have a high fraction of energy remaining in the jet. The two cases have a different inertia ratio between jet and ISM (case A: $\eta = 28.6$; case D: $\eta = 0.8$). The reason of this low transfer is than different in origin: for case A we expect the high inertia ratio to cause the jet to travel freely despite the large surface of interaction due to the precession. For case D on the other hand, the inertia ratio should lead to more interaction. But the surface of interaction is really small compare to all other cases. Without precession we stay with a Ω factor correction to the 1D Marti equation (see section 3.1) equal to 1. But where the cocoon region receives almost no energy in case D, almost 20% of the deposit energy go to the cocoon for case A. If we sum this with the contribution to the SISM region we see that about 40% of the deposit energy is transferred from the jet to the medium for case A, where this is only about 20% for case D. Again we see that the precession results in an increased interaction between the jet and its surroundings.

As in Monceau-Baroux et al. (2012), for the non-precessing case D, we observe (figure 8) the formation of a structured beam for the jet with material of the medium being pushed by the head of the jet as by a piston. Due to an extreme adiabatic expansion behind the material of the jet, this outer layer of the beam have low density and

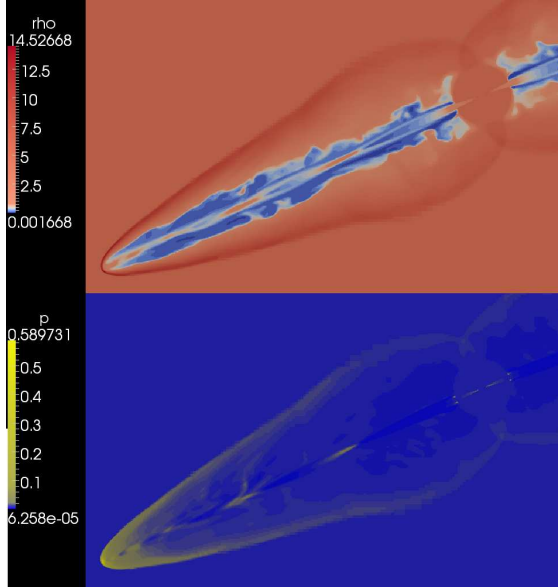


Fig. 8. Top: Density plot of one jet of case D. Bottom: Pressure plot of one jet of case D. Formation of a structured beam for the jet by pushing material from the ISM by the head of the jet, as by a piston. Due to adiabatic expansion, the density in that outer layer is low, whereas density and pressure build up in front of the head of the jet. Formation of standing recollimation shocks along the path of the jet.

pressure. Whereas pressure and density build up in front of the head of the jet.

Other known features of relativistic jets can be observed for case D: internal recollimation shock, formation of a strong interaction at the head of the jet. We recall that most of the kinetic energy is transformed into thermal energy at that position. Secondary transfer takes place throughout the instabilities that appear at the head of the jet and are then advected along it.

3.3. Radio mapping

Following the method described in section 2.2 we realised 4 different radio maps for cases A, B, C and D. This radiomaps can be seen on figure 9 and 10. All cases are made so the phase of the precession period is similar. The radio map of case A, B and C are compared to the observations to test the model. Case D is a good example of the radio emission for a relativistic standing jet. We know the distance to SS433, estimated to be 5.5 kpc. We can then scale our radio map to find the correspondence between the projected arcsec and the physical distance in parsec. We note again that for the virtual radio map, we used the pressure as a proxy for the magnetic field. As a result we can only compare the appearance of the jet features and not their absolute values, such as their intensity. On the right part of figure 9, from Roberts et al. (2008), we have the intensity contours at 4.80 GHz, made from data taken over 1998 March 5-7.

Did you ask him to take the plot? Overplotted is the canonical kinematic model assumed for SS433, with plus signs and circles indicating oncoming and receding parts, respectively. We labelled with I, II, III and IV individual bright features which appear on the different figures. Note that

those components, albeit slightly different due to the tilt to the line of sight (80° with respect to the axis of precession), are present for both jets. For case B, second from the left part of figure 9, only component I is visible. Component V however, does not appear on both simulation A, B and C, as on different observations at different frequencies of SS433. In Roberts et al. (2008), the feature is present at 4.80 GHz, less extended from 1.415 to 1.665 GHz and completely absent at 14.94 GHz. Doolin & Blundell (2009) studies the hypothesis that this feature may be emitting plasma from the circumbinary disks of SS433. Another hypothesis would be that this feature is linked with backflows at the meeting point of the cocoons inflated by both jets. But we found in none of our simulated cases any evidence for this.

We note that the relative intensities of components I, II, III and IV are different between the observations and our own radio maps. For case A, they are located in the same position whereas, in case B they are located further away from the source and in case C they are situated close to the precession axis. We note that the locations of these components are solely depending on the dynamics of the jet, where their intensities are strongly dependent on the radiation mechanism. On the observational map, the canonical kinematic model for SS433 is overplotted. We note that the position of the model and the position of the actual bright components are off even in the observations. This mismatch increases with the distance to the source of the jet. The reason is that this kinematic model does not take into account the increased interaction between the jet and the ISM due to the precession, and the previous deceleration history, which we obtain self-consistently. By opposition to the ballistic behaviour of this model our simulation case A therefore gives a better match to the observations than the pure canonical model, by taking actual dynamics into account. Case B however results in a bad match with the radio components getting away from the source too fast as is case C where components stay close to the precession axis. Both case A and B are corrected for Doppler Effect. For case A and C, this plays little role as we see almost no difference in intensity between the radio component and their mirror in the lower part of the domain. This is expected of the low velocity of the jet. By comparison, for case B, the radio components in the top part of the domain are much brighter than their counter-part in the lower part of the domain as the higher Lorentz factor would suggest. If we now compare with the observation, we see that for SS433, there is little difference in intensity between the top and bottom radio components. Both arguments, distances and symmetry of the radio components, discarded the possibility for a set of parameters including a value for γ different from $0.26c$. In their model, Zavala et al. (2008), use a 10° degree precessing angle to reproduce the interaction of SS433 with the supernova remnant W50 on the scales of 20 pc. The motivation for case C was to see if such an angle could also reproduce the radio observation at sub-parsec scale. As shown, this is not the case. We conclude that either between the two scales there is recollimation of the precessing jet, or the angle of precession of SS433 has evolved during its history.

The radio map of case D shows different features known from the study of relativistic jets: due to the inclination of the jet-axis with respect to the line of sight, the Doppler effect boosts the emission from the jet pointing towards the observer and lowers the one pointing away from the

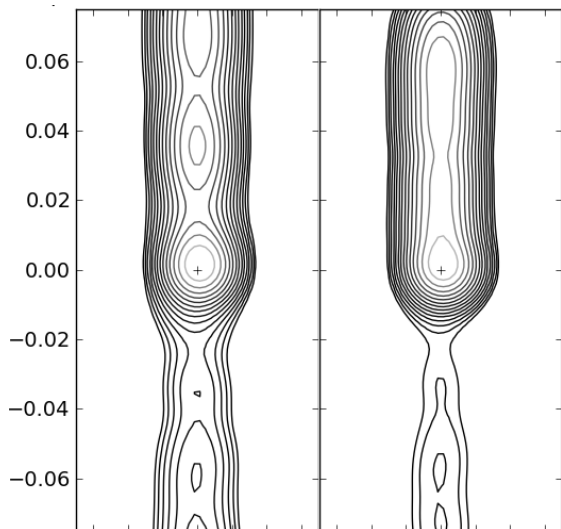


Fig. 10. Left: Radio map from the simulation, Case D, angle to the line of sight 85° . Right: Angle to the line of sight 78° . With distance units in parsec. Object is estimated to be at a distance of 5.5 kpc.

observer. We can see this pattern for example in the observation of 3C 296 (see Laing et al. (2006)). For statically injected relativistic jets, standing recollimation shocks are known to form along the path of the jet. Case D is no exception as shown on figure 8. These shocks are discussed to be the site of particle acceleration within the jet. This would result in the brightening of those shocks and explain the bright blobs observed along the path of relativistic jet as in M87 and Cyg A. We recall that we do not account in our simulation for acceleration of particles in shocks (see section 2.2). Nevertheless we observe on our radio map of case D (right hand side of figure 10) the appearance of such a bright spot. This would hint that the compression of the fluid at recollimation shocks could already suffice for the formation of the emission blobs.

On the other hand, our model for radiation can still be improved, with an important step to drop the frozen-in assumption and to evolve the magnetic field dynamically. This could be done at first by assuming that it does not have any retro-action on the dynamics. This would prevent us from moving to a full MHD model and cutting down computational cost.

4. Conclusion

We have two separates set of conclusions for this work. The first ones are made on fundamental hydrodynamics processes. We show how the precession of a jet, and its Lorentz Factor, change the interactions with its surroundings, and thus the energy exchange between the jet and the medium. The second series of conclusions are made on the observations of the radio maps made from our simulations cases. They show which set of parameters seems to fit actual VLA observation better.

Our hydrodynamic study had two directions: a parametric study was evaluating the impact of the variation of the Lorentz factor. We recall that our kinetic flux was constant the Lorentz factor being linked to the density of the

jet through equation 4. The first observations is that case A with the lower Lorentz factor ($\gamma = 1.036$) is over dense compared with its surroundings. This result in less interaction as the jet propagated easily in the medium. Energy quantification shows that most of the kinetic and thermal energy stay in the jet itself with less than 40% of the energy in the remaining region of the simulation, ISM and cocoon. By comparison, case B, with the higher Lorentz factor ($\gamma = 1.87$) shows strong interaction. This jet is under dense compared to the ISM and we observe more than 70% of the energy being transferred from the jet to the surroundings. Finally case D, with its fixed propagation direction, propagated almost freely, less than 30% of the energy is transferred with almost nothing to the cocoon. As for standing jet in AGN or XRB, the density ratio between the jet and the ISM plays a fundamental role in the interaction between the jet and its surroundings. We recall that the three main mechanisms of interaction, or energy transfer, is the exchange of kinetic to thermal energy at the front shock of the jet. For non precessing jet, this mainly tack place at the mach disk of the jet. The second mechanism is the mixing of material from the jet and the surroundings through instabilities. Finally shocks formed by the jet propagation and propagating in the surroundings can heat it. On the other hand the precession increases dramatically those interactions. We explained this through two aspect: the first mechanism is not anymore present at the jet head only. We recall that for standing cases its completely dominating the energy transfer (see Monceau-Baroux et al. (2012)). Here this particular interaction is present all along the jet. Also in standing case the front of interaction is only slightly larger than the interaction surface of the jet (see Walg et al. (2013)). Here this front is over extended by the precession and the jet interacts with quite a large portion of its surroundings. As the density ratio is concerned, we noted that the helical shape of under-dense jets does not survive for as long. This would favor an over-dense jet models as our case A with a Lorentz factor of $\gamma = 1.036$ or injection velocity $v_j = 0.26c$. It is also interesting to noted that we do not know of any quickly precessing AGN jets which are widely admitted as being under dense.

Our second set of observations were more directly aims to reproduce SS433 radio observations. We briefly point out how radio map of standing case D was giving some insight on relativistic jets. We shown how the hydrodynamics conditions of the jet alone could already explained some of the features observed in space: bright radio blobs along the path of the jet could come from pinching of the matter of the jets at the position of recollimation shocks. We again confirmed the scenario of case A. It visually reproduces quite well the VLA radio observations of SS433 with bright radio components located at similar distances. On the other hand we noted a slight under estimation of the interaction by the canonical kinematic model. We see on the VLA data (figure 9) that it over estimates the distance of propagation of the fluid element. Our model fit the observation better and we see that the reason is that by following completely the full 3D dynamic of the jet, we follow better those interactions. This is a result also found by a different approach by Panferov (2013) who use an analytic approach to find that to fit the observation, the kinematic model has to be corrected for deceleration.

In upcoming work we plan to go closer to the source and study possible time dependant variability of the jet

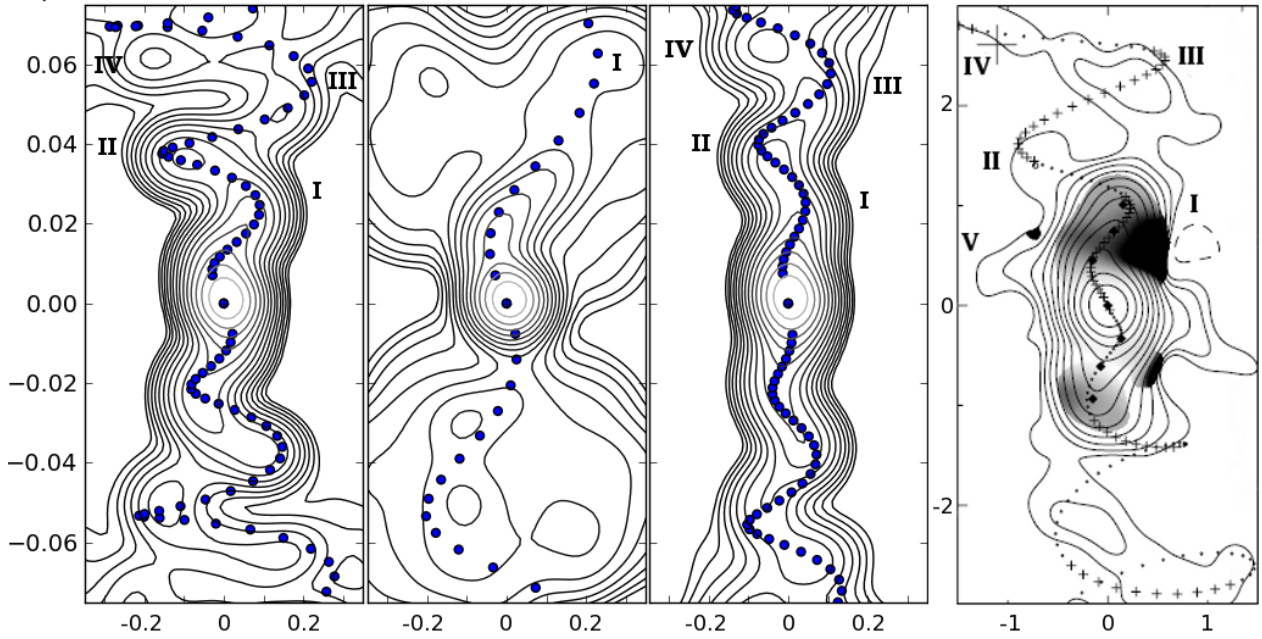


Fig. 9. Left to right: Radio map from simulations Case A, Case B and case C. Unit are in parsec, bject is estimated to be at a distance of 5,5 kpc. On all graphs are overplots the kinematic model with parameters corresponding to the case. Right: VLA image of the microquasar SS433 in the constellation Aquila, CREDIT Roberts et al. (2008), unit are in arcsecond. Is overplot the kinematic model for SS433. Both simulated radiomap and observations contours have steps of factors of $\sqrt{2}$.

flux. This with the additionnal aim to reproduce the time dependant VLBA observations where blobs are seen, shouting out of the source.

Acknowledgements. For part of the simulations, we used the infrastructure of the VSC-Flemish Supercomputer Center, funded by the Hercules Foundation and the Flemish Government -department EWI. Part of the simulations used the infrastructure of the Jade - CINES French supercomputer Centre, with a funding from the European project HPC-EUROPA2. Additional simulations were run on Curie and Fermi supercomputers thanks to the PRACE research infrastructure grant SWEET. We acknowledge financial support from FWO-Vlaanderen, grant G.0238.12 and from project GOA/2009/009 (KU Leuven).

References

Blumenthal, G. R. & Mathews, W. G. 1976, *ApJ*, 203, 714
 Blundell, K. M., Bowler, M. G., & Schmidtobreick, L. 2008, *ApJ*, 678, 47
 Borisov, N. & Fabrika, S. N. 1987, *SvA*, 13, 487
 Bowler, M. G. 2013, *A&A*, 556, 149
 Brinkmann, W., Kotani, T., & Kawai, N. 2005, *A&A*, 431, 575
 Camus, N. F., Komissarov, S. S., Bucciantini, N., & Hughes, P. A. 2009, *MNRAS*, 400, 1241
 Collins, II, G. W. & Newsom, G. H. 1979, *Nat*, 280, 474
 Crampton, D. & Hutchings, J. B. 1981, *ApJ*, 251, 604
 Doolin, S. & Blundell, K. M. 2009, *ApJ*, 698, 23
 Dubner, G. M., Holdaway, M., Goss, W. M., & Mirabel, I. F. 1998, *AJ*, 116, 1842
 Fabian, A. C. & Rees, M. J. 1979, *MNRAS*, 187, 13
 Fragos, T., Lehmer, B. D., Naoz, S., Zezas, A., & Basu-Zych, A. R. 2013, *Ark. Astron.*, 1306.1405
 Hjellming, R. M. & Johnston, K. J. 1981, *ApJ*, 246, 141
 Katz, J. I., Anderson, S. F., Grandi, S. A., & Margon, B. 1982, *ApJ*, 260, 780
 Keppens, R., Meliani, Z., Marle, A. J. V., et al. 2012, *JCoPh*, 231, 718
 Koren, B. 1993, *Numerical Methods for Advection-Diffusion Problems*, ed. C. B. Vreugdenhil & B. Koren, Afdeling Numerieke

Wiskunde: Report NM (Centrum voor Wiskunde en Informatica), 117–138
 Krivosheyev, Y. M., Bisnovatyi-Kogan, G. S., Cherepashchuk, A. M., & Postnov, K. A. 2009, *MNRAS*, 394, 1674
 Laing, R. A., Canvin, J. R., Bridle, A. H., & Hardcastle, M. J. 2006, *MNRAS*, 372, 510
 Livio, M. 2000, in *American Institute of Physics Conference Series*, Vol. 522, American Institute of Physics Conference Series, ed. S. S. Holt & W. W. Zhang, 275–297
 Margon, B. 1984, *ARA&A*, 22, 507
 Margon, B., Grandi, S. A., Stone, R. P. S., & Ford, H. C. 1979, *ApJ*, 233, 63
 Markoff, S. 2006, in *VI Microquasar Workshop: Microquasars and Beyond*
 Marshall, H. L., Canizares, C. R., Hillwig, T., et al. 2013, *ApJ*, 775, 75
 Marti, M., Muller, E., Font, J. A., Ibanez, J. M., & Marquina, A. 1997, *ApJ*, 479, 151
 Meliani, Z., Keppens, R., & Giacomazzo, B. 2008, *A&A*, 491, 321
 Milgrom, M. 1979a, *A&A*, 76, 3
 Milgrom, M. 1979b, *A&A*, 78, 17
 Milgrom, M., Anderson, S. F., & Margon, B. 1982, *ApJ*, 256, 222
 Monceau-Baroux, R., Keppens, R., & Meliani, Z. 2012, *A&A*, 545, A62
 Muller, E. & Brinkmann, W. 2000, in *IAU Symposium*, Vol. 195, *Highly Energetic Physical Processes and Mechanisms for Emission from Astrophysical Plasmas*, ed. P. C. H. Martens, S. Tsuruta, & M. A. Weber, 415
 Panferov, A. A. 2013, *Ark. Astron.*, 1306.3599
 Paragi, Z., Vermeulen, R. C., Fejes, I., et al. 1999, *Nar*, 43, 553
 Porth, O., Komissarov, S. S., & Keppens, R. 2013, *MNRAS*
 Roberts, D. H., Wardle, J. F. C., Lipnick, S. L., Selesnick, P. L., & Slutsky, S. 2008, *ApJ*, 676, 584
 Safi-Harb, S. & Ogelman, H. 1997, *ApJ*, 483, 868
 Silk, J. & Rees, M. J. 1998, *A&A*, 331, 1
 Spencer, R. E. 1979, *Nat*, 282, 483
 Stephenson, C. B. & Sanduleak, N. 1977, *BAAS*, 33, 459
 Tóth, G. & Odstrčil, D. 1996, *JCoPh*, 128, 82
 Walg, S., Achterberg, A., Markoff, S., Keppens, R., & Meliani, Z. 2013, *MNRAS*, 433, 1453

Zavala, J., Velázquez, P. F., Cerqueira, A. H., & Dubner, G. M. 2008,
MNRAS, 387, 839